

# A feasibility study on the photometric detection of quiescent black hole X-ray binaries

Jorge Casares<sup>1,2\*</sup>, Manuel A.P. Torres<sup>1,2,3†</sup>

<sup>1</sup>*Instituto de Astrofísica de Canarias, 38205 La Laguna, Tenerife, Spain*

<sup>2</sup>*Departamento de Astrofísica, Universidad de La Laguna, E-38206 La Laguna, Tenerife, Spain*

<sup>3</sup>*SRON, Netherlands Institute for Space Research, Sorbonnelaan 2, 3584 CA, Utrecht, The Netherlands*

Accepted XXX. Received YYY; in original form ZZZ

## ABSTRACT

We investigate the feasibility of detecting quiescent black hole X-ray binaries using optical photometric techniques. To test this we employ a combination of  $r$ -band and  $H\alpha$  filters currently available at the Roque de los Muchachos Observatory. Photometric observations of four dynamical black holes (GRO J0422+320, A 0620-00, XTE J1118+480 and XTE J1859+226) at  $\text{SNR} \gtrsim 35$ -50, supplemented with near simultaneous spectroscopic data, demonstrate that it is possible to recover the FWHM of the  $H\alpha$  emission line to better than 10% for targets with a wide range of line EWs and down to magnitude  $r \sim 22$ . We further explore the potential of our photometric system to disentangle other populations of compact stars and  $H\alpha$  emitters. In particular, we show that *HAWKs*, a survey designed to unveil quiescent black holes, will also provide a detailed census of other Galactic populations, most notably short period (eclipsing) cataclysmic variables, neutron star X-ray binaries and ultra-compact binaries.

**Key words:** accretion, accretion discs – X-rays: binaries – stars: black holes – (stars:) novae, cataclysmic variables – stars: emission-line, Be – techniques: photometric

## 1 INTRODUCTION

In the era of gravitational wave (GW) discoveries (Abbott et al. 2016a,b, 2017a,b,c) the study and characterisation of accreting black holes (BH) in the Milky Way remains a topic of important strategic interest. These systems provide us with a reference sample of BH properties (e.g. space density, masses, spin) stemmed from well defined evolutionary channels at high metallicity (see Tauris & van den Heuvel 2006). And yet, our knowledge on the formation of black hole X-ray binaries (BHXBs) is far from complete, with crucial issues that need to be solved. Just to mention a few, it is not well understood how a low mass companion star can possibly survive the common envelope phase and a supernova (SN) explosion, resulting in the observed numbers of BHXBs (e.g. Podsiadlowski, Rappaport & Han 2003; Wang et al. 2016). It is uncertain whether BHs receive a natal kick or are formed by implosion (Repetto et al. 2017; Mirabel 2017; Casares, Jonker & Israelian 2017). Is also unclear if standard BHXB formation channels can produce BHs heavier than  $\sim 15 M_{\odot}$  (c.f. Belczyński et al. 2010) or whether SN physics is responsible for the  $\sim 2$ -5  $M_{\odot}$  mass gap between

neutron stars (NS) and BHs hinted by observations (Fryer et al. 2012; Ugliano et al. 2012).

With the exception of Cyg X-1 and MWC 656 (a Be/BH binary that may end up in a BH/NS merger and thus a source of GWs; Casares et al. 2014; Grudzinska et al. 2015) the great majority of accreting BHs in the Galaxy have been detected through dramatic X-ray outbursts. About 60 of these, so-called, BH *X-ray transients* have been discovered in five decades of X-ray surveys (see the BlackCat catalogue in Corral-Santana et al. 2016) but only 17 hold dynamical confirmation (i.e. mass function greater than  $\sim 3 M_{\odot}$ ), owing to difficulties in measuring the spectrum of the companion star at very faint quiescent luminosities (Casares & Jonker 2014). Our knowledge of their fundamental parameters (orbital period, masses, space velocities, etc.), and thus on the formation and evolution of BHXBs as a population, is clearly jeopardised by limited statistics. Therefore, it is of paramount interest to explore new routes to unveil the hidden population of hibernating (quiescent) BHXBs.

Notwithstanding these limitations, dynamical information can still be extracted from scaling relations based on the properties of the disc  $H\alpha$  emission line (Casares 2015, 2016; Papers I and II hereafter). In particular, building upon the FWHM- $K_2$  empirical relation, presented in Paper I, we have developed a new approach to single out quiescent BHXBs

\* E-mail: jorge.casares@iac.es

† E-mail: manuel.perez.torres@iac.es

among the myriad of  $H\alpha$  emitters. In fact, blind  $H\alpha$  surveys of the Galactic plane, such as IPHAS, the *INT Photometric  $H\alpha$  Survey of the Northern Galactic Plane* (Drew et al. 2005)) have successfully increased the statistics of  $H\alpha$  emitting populations, including young stellar objects (YSOs), cataclysmic variables (CVs), symbiotic stars and others, but have so far failed to discover quiescent BHXBs. This is unsurprising given the extremely low density of the latter and the lack of clear optical signatures that set them apart from other populations of  $H\alpha$  emitters. A different strategy, the selection of  $H\alpha$  sources with weak X-ray emission from Chandra surveys of the Galactic Bulge and Plane (Grindlay et al. 2005; Jonker et al. 2011) has proved most sensitive to magnetic CVs and coronal stars but, again, not to quiescent BHXBs (see e.g. Rogel et al. 2006; Torres et al. 2014; Wevers et al. 2017).

Alternatively, in Casares (2018) (hereafter Paper III), we propose the full-width-half-maximum (FWHM) of the  $H\alpha$  line as an efficient diagnostic to discriminate BHXBs from other  $H\alpha$  emitting objects. Paper III presents a proof-of-concept on how  $H\alpha$  widths can be extracted from imaging techniques and devises a new photometric system, optimised to measure equivalent widths (EWs) and FWHMs, the two basic line-profile parameters. It is based on three  $H\alpha$  filters with squared response functions of increasing width but the same central wavelength. This allows breaking the degeneracy between EW and reddening (Drew et al. 2005; Witham et al. 2006), and thus a unique determination of both EW and FWHM line values. Furthermore, a filter cycling strategy is proposed to mitigate the effect of flickering variability in FWHM determinations while  $\sim 1$  kilo square degree survey (*HAWKs*, the  *$H\alpha$  Width Kilo-degree survey*) at signal-to-noise ratio (SNR)  $\sim 50$  and depth  $r = 22$  is set out for the discovery of, at least,  $\sim 50$  new hibernating BHXBs. Here in this paper we present a feasibility study to demonstrate that this strategy allows the recovery of FWHM values in quiescent BHXBs to better than 10% accuracy, through photometric observations of a sample of quiescent BHXBs (Section 3). The sample embraces BHXBs with a large range of EW and FWHM values, down to very faint magnitudes  $r \sim 22$ . In Section 4 we summarize the results and lay out the prospects of this photometric system for isolating other populations of compact stars and  $H\alpha$  emitters.

## 2 OBSERVATIONS AND DATA REDUCTION

We have employed the Auxiliary-port CAMera (ACAM) on the 4.2 m William Herschel Telescope (WHT) at the Roque de los Muchachos Observatory in La Palma to obtain images of five quiescent BHXBs: Swift J1357-0933 on the night of 16 Feb 2018, GRO J0422+320, A 0620-00 and XTE J1118+480 on 17 Feb 2018 and XTE J1859+226 on 20 June 2018. We name these targets J1357, J0422, A0620, J1118 and J1859 hereafter. The images were obtained with the NOT29 broad  $H\alpha$  filter ( $\lambda_{\text{central}}=6560 \text{ \AA}$ , FWHM=113  $\text{\AA}$ ), the NOT21 narrow  $H\alpha$  filter ( $\lambda_{\text{central}}=6564 \text{ \AA}$ , FWHM=33  $\text{\AA}$ ) and the r-band filter MR661 ( $\lambda_{\text{central}}=6608 \text{ \AA}$ , FWHM=798  $\text{\AA}$ ) from OASIS, a former Isaac Newton Group (ING) instrument currently decommissioned. The latter has been chosen among a possible list of ING r-band filters because it has the closest effective wavelength to the  $H\alpha$  rest wavelength, a critical

requirement of our photometric system (see Paper III for details). The filters are hereafter referred to as  $H\alpha_b$ ,  $H\alpha_n$  and r and their transmission profiles<sup>1</sup> are plotted in Fig. 1.

The r-band filter has a small clear aperture of 25mm and it was mounted in the ACAM slit unit, located at the focal-plane of the instrument. By doing this we ensure that the filter will not vignette the light beam although the available field-of-view (FOV) becomes severely limited, with only the central 1.1 arcmin (diameter) unvignetted. The two  $H\alpha$  filters were instead mounted in filter wheel positions, at the pupil-plane of the instrument. This introduces a blueshift in the effective wavelength with distance from the optical axis, but the effect is negligible within the central 1.1 arcmin area of overlap between our three filters i.e. the effective FOV for useful scientific observations. The 2Kx4K EEV CCD was windowed to the central part (of approximately 1.6 arcmin side) resulting in a readout time of only two seconds.

Continuous r/ $H\alpha_b$ / $H\alpha_n$  cycles were performed on every BH target. The number of cycles and integration times were initially designed to reach a final (average) SNR  $\geq 50$  in every filter, a requirement defined by Paper III. Four such cycles were obtained for J0422 between 20:17-20:57 UT, five for A0620 between 21:05-21:18 UT, 16 cycles for J1118 between 22:16-23:30 UT and four cycles for J1859 between 02:03-03:10 UT. The J1357 observations were performed just before morning twilight and consisted of a single r/ $H\alpha_b$ / $H\alpha_n$  cycle. The nights of 16 and 17 Feb were clear and photometric, with seeing around 1 arcsec, except for the block of J1118 observations when seeing degraded to  $\sim 2.5$  arcsec, with rapid variations caused by wind gust conditions. The night of 20 June was also photometric, with excellent seeing of 0.6 arcsec.

Near simultaneous spectroscopic observations of J0422, A0620, J1118 and J1859 were programmed with the Optical System for Imaging and low-Intermediate-Resolution Integrated Spectroscopy (OSIRIS) at the 10.4m Gran Telescopio Canarias (GTC). We employed grism R1000B and a 1.0 arcsec slit to cover the wavelength range 3780-7880  $\text{\AA}$  at 6.4  $\text{\AA}$  resolution ( $=292 \text{ km s}^{-1}$  at  $H\alpha$ ). A spectrum of the flux standard BD+52 913 was also acquired with a slit width of 2.5 arcsec for the purpose of flux calibration. The slit was oriented at parallactic angle to minimize the impact of atmospheric refraction on our flux calibration. The J0422 spectroscopy spans over 95% of the corresponding photometric window while the A0620 and J1859 spectra cover 85% and 74% of their photometric baselines, respectively. A technical failure during the GTC observations of J1118 produced a 41 min gap with no useful data which results in only 45% simultaneous coverage. The J1357 photometry could not be supported by simultaneous GTC spectroscopy.

r/ $H\alpha_b$ / $H\alpha_n$  images of two late-type photometric Landolt stars (SA95 15 & 16, Landolt 1992) and the A0V star BD+30 2355 were also obtained on the night of 17 Feb. The latter was acquired to provide a zero point in the photometric calibration tied to the Vega system. Low resolution spectra of the photometric standards were further acquired with

<sup>1</sup> The transmission curves are available from <http://www.not.iac.es/instruments/filters/curves-ascii/29.txt>, <http://www.not.iac.es/instruments/filters/curves-ascii/21.txt> and <http://catserver.ing.iac.es/filter/filtercurve.php?format=txt&filter=585>

the V400 grism available on the filter-wheel unit of ACAM. These ACAM spectra cover the wavelength range 5020–9280 Å at  $\sim 495 \text{ km s}^{-1}$  resolution. The aim was to compute synthetic magnitudes with the nominal transmission curves of our filters, to be compared to the real magnitudes provided by the actual filters. An ACAM spectrum of the spectroscopic flux standard Feige 15 (plus a set of  $r/H\alpha_b/H\alpha_n$  images) was also obtained for the purpose of flux calibrating the spectra of the photometric standards. Our list of standards also includes a star in the field of A0620, USNO B1.0 0896-0086799, which fortuitously lay in the OSIRIS slit. We name this star A0620-C1 hereafter. An observing log, with details on integration times, is presented in Table 1.

The spectroscopic data were processed in the standard way with debias, flat-field correction and optimal spectral extraction using STARLINK/PAMELA routines (Marsh 1989). Observations of CuNe+CuAr (ACAM) and HgAr+Ne (OSIRIS) lamps were employed to derive a pixel-to-wavelength calibration through a 4th order polynomial fit to more than 28 lines across the entire wavelength range. Small flexure corrections, obtained from the position of the O I 5577.34 and 6300.30 sky lines, were applied to individual spectra in order to match the laboratory positions within  $1 \text{ km s}^{-1}$ . Figure 1 displays the OSIRIS (average) spectra of the BHXBs and the ACAM spectra of the standard stars, together with the transmission curves of our filters. We have assigned an approximate spectral classification for the Landolt photometric standards based on the relative depth of the spectral lines and their photometric (B–V) colour.

The photometric data acquired with ACAM were reduced in the following way: for each program object and standard star, images were bias subtracted, flat-field corrected and aligned using IRAF<sup>2</sup> tasks. Stellar fluxes were extracted using aperture photometry because none of our targets is blended with nearby stars. Aperture photometry was then performed on each image using the DAOPHOT package to derive instrumental magnitudes for our targets, their field stars as well as the Landolt standards. Different apertures were chosen according to the image quality at each filter. Aperture corrections were subsequently calculated with a curve-of-growth analysis using DAGROW (Stetson 1990) and applied to the instrumental magnitudes.

### 3 ANALYSIS

Following usual convention, we decide to refer our magnitudes to the Vega based zero magnitude scale. For example, the magnitude of a given target in the  $H\alpha_b$  filter will be provided by

$$m_{H\alpha_b} = -2.5 \log \left( \frac{F_{H\alpha_b}}{F_{H\alpha_b}^0} \right) \quad (1)$$

where  $F_{H\alpha_b}$  is the target’s flux while  $F_{H\alpha_b}^0$  that of the A0V star BD+30 2355. Note that, by adopting this definition, the magnitudes (and colours) of a A0V standard star are

<sup>2</sup> IRAF is distributed by the National Optical Astronomy Observatories, which are operated by AURA, Inc., under cooperative agreement with the National Science Foundation.

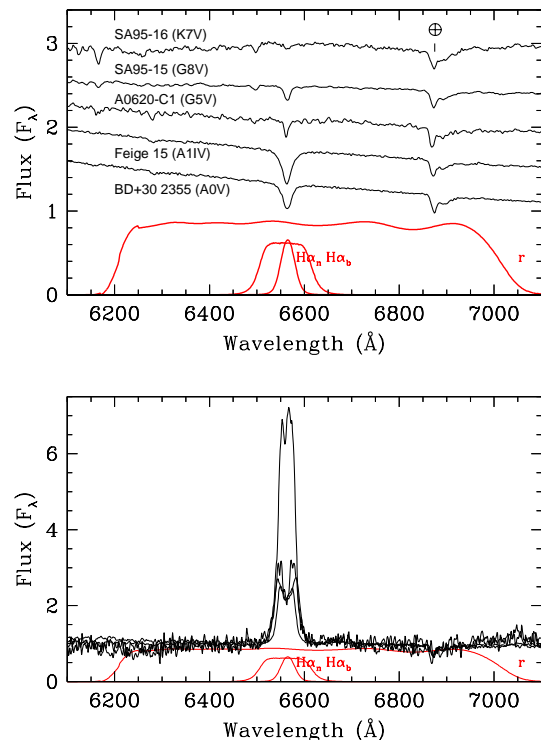


**Figure 1.** Top: WHT+ACAM spectra of standard stars, together with the transmission curves of the  $r$ -band and the two  $H\alpha$  filters. The GTC+OSIRIS spectrum of a comparison star in the field of A 0620-00, broadened to the same resolution of the ACAM spectra, is also displayed. All the spectra have been normalized to the continuum at  $H\alpha$ . For the sake of display, relative vertical offsets have been applied to the spectra. Bottom: Averaged GTC+OSIRIS spectra of the four BHXBs. These spectra have also been normalized to the continuum at  $H\alpha$ .

set to be zero. As a sanity test, we start by comparing the observed magnitudes of the standard stars with their synthetic magnitudes. The latter are obtained from equation 1, using simulated fluxes computed through the convolution of the filter’s response ( $T_{H\alpha_b}$ ) with the observed spectra i.e.

$$F_{H\alpha_b} = \int T_{H\alpha_b} \times f_{\lambda} d\lambda \quad (2)$$

and

$$F_{H\alpha_b}^0 = \int T_{H\alpha_b} \times f_{\lambda}^0 d\lambda \quad (3)$$

where  $f_{\lambda}$  and  $f_{\lambda}^0$  are the spectra of the target and BD+30 2355, respectively. In all cases, both the observed spectra and filter response curves have been re-sampled to a common bin size of  $1 \text{ \AA pix}^{-1}$ . Table 2 lists the synthetic and observed photometric colours of the four standard stars plus A0620-C1. The mean differences between photometric and synthetic colours ( $m_r - m_{H\alpha_b}$ ) and ( $m_{H\alpha_b} - m_{H\alpha_n}$ ) are  $0.03 \pm 0.05$  and  $0.02 \pm 0.03$  respectively. These values drop to  $0.01 \pm 0.03$  and  $-0.001 \pm 0.019$  if we restrict ourselves to the

three late-type standards. This indicates that the A-type stars are responsible for most of the difference, probably caused by the ACAM spectra not properly resolving the core of the broad  $H\alpha$  absorption profiles. In any case we consider these deviations acceptable, given our limitations in spectral resolution and uncertainties in flux calibration. It should be noted that the photometric  $m_r$  values listed in the second column of Table 2 are purely instrumental. Comparison with calibrated r-band magnitudes indicates that the former are underestimated by  $\approx 1.1$  mag.

### 3.1 Calibration of Photometric EWs and FWHMs

As explained in appendixes B and C of Paper III, for the case of perfect ideal filters (i.e. those with squared response curves with 100% peak transmission and identical central wavelength) it is possible to derive the EW and FWHM of an  $H\alpha$  line through equations

$$EW^* = \frac{W_r \times \left( \frac{F_{H\alpha_b}}{F_r} \right) - W_{H\alpha_b}}{1 - \left( \frac{F_{H\alpha_b}}{F_r} \right)} \quad (4)$$

$$FWHM^* = \frac{EW^*}{\left( \frac{EW^* + W_{H\alpha_b}}{W_{H\alpha_n}} \right) \times \left( \frac{F_{H\alpha_n}}{F_{H\alpha_b}} \right) - 1} \quad (5)$$

where  $EW^*$  and  $FWHM^*$  are the EW and FWHM values, as measured from the filters,  $W_r$ ,  $W_{H\alpha_b}$ ,  $W_{H\alpha_n}$  the equivalent widths of the r-band,  $H\alpha_b$  and  $H\alpha_n$  filters and  $F_{H\alpha_b}$ ,  $F_{H\alpha_n}$ ,  $F_r$  the associated fluxes. For the case of real filters, however, variations in filter response curves and central wavelength relative to those of ideal filters will introduce deviations between the  $EW^*$  and  $FWHM^*$  measurements and the true line EW and FWHM values. For the simulated filters presented in Paper III, we showed that simple calibration constants can account for the observed deviations (eqs. B4 and C3 in Paper III). Instead, we find here that the MR661, NOT29 and NOT21 filters do require a quadratic calibration term i.e.

$$EW_{ph} = EW^* (C_1 + C_0 EW^*) \quad (6)$$

$$FWHM_{ph} = FWHM^* (C_2 + C_3 FWHM^*) \quad (7)$$

where  $C_0 - C_3$  are the calibration constants and  $EW_{ph}$  and  $FWHM_{ph}$  our best photometric determination of the line EW and FWHM. We note that higher order polynomial terms do not lead to a significant improvement in the calibration of the photometric parameters. As in Paper III, we derive the calibration constants by comparing EW and FWHM values from a grid of simulated double-peaked emission  $H\alpha$  profiles with synthetic values obtained through convolution with the filter transmission curves and equations 4-7, with  $W_r=674 \text{ \AA}$ ,  $W_{H\alpha_b}=73 \text{ \AA}$  and  $W_{H\alpha_n}=25 \text{ \AA}$ . This results in  $C_0 = 0.0009$ ,  $C_1 = 1.8588$ ,  $C_2 = 0.4200$  and  $C_3 = 0.0003$ .

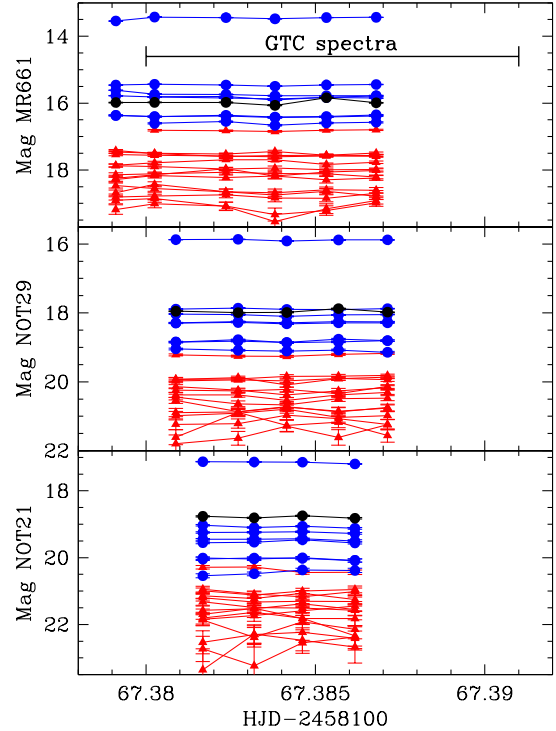


**Figure 2.** Light curves of A 0620-00 (black solid circles) and 22 stars in the 1.1 arcmin field of view. Displayed magnitudes are instrumental. As a reference, calibrated r-band magnitudes correspond to  $\text{mag}(\text{MR661})+1.1$ . Blue solid circles indicate field stars with  $\text{SNR} \geq 50$  in the three filters, the remaining are marked by red solid triangles and no longer considered. Three field stars lie in the outer vignettted area of the first (offset) image of the MR661 filter and, therefore, are not displayed in the top panel. The last NOT21 image is corrupted by CCD cross-talk and has been rejected. 85% of the photometric window is covered by GTC spectroscopy.

### 3.2 Photometric EWs and FWHMs

We can now apply the calibrated relations eq. 4-7 to our ACAM photometry and derive  $EW_{ph}$  and  $FWHM_{ph}$  values for each BHXB. As explained in Section 2, the photometric data were acquired as a sequence of consecutive  $r/H\alpha_b/H\alpha_n$  cycles so to average out flickering variability, typical of quiescent BHXBs (Zurita et al. 2003). This leads to a set of quasi-simultaneous light curves for each object in the three filters. An example is presented in Figure 2, where the light curves of A0620 and 22 field stars are displayed. Stars with  $\text{SNR} < 50$  in any filter are rejected by a clipping process. Time averaged magnitudes in every filter were subsequently computed as the weighted mean of individual data points, and the resulting photometric colours of BHXBs transformed into flux ratios and introduced into equations 4-7 to derive  $EW_{ph}$  and  $FWHM_{ph}$  values.

To assess how reliable these photometric measurements are we have also extracted EW and FWHM values from the near-simultaneous GTC spectra. EWs were obtained by integrating the  $H\alpha$  flux in the (continuum normalized) spectra,



while FWHMs came from single Gaussian fits to the  $H\alpha$  profiles. Following Paper I, we adopt the mean and standard deviation in the distribution of individual values. A comparison between the photometric and spectroscopic determinations of EW and FWHM values is presented in Figure 3 and Table 3. The first two columns of Table 3 provide additional information on the accumulated  $m_r$  magnitudes and SNR. We stress again the fact that the quoted  $m_r$  magnitudes are instrumental. Calibrated  $r$ -band (continuum) magnitudes are given in the third column and have been estimated through  $r = m_r + 1.1 + 2.5 \log(1 + EW/W_r)$ , where the latter term accounts for the contribution of the  $H\alpha$  flux to the  $m_r$  magnitude. For completeness, Table 3 and Figure 3 also include the  $EW_{ph}$  and  $FWHM_{ph}$  determinations for J1357, as obtained from a single photometric observation. Due to the lack of simultaneous GTC spectroscopy, however, we here adopt spectroscopic values from spectra obtained in 2014 by Mata Sánchez et al. (2015). These values are fully consistent with an earlier determination reported in Torres et al. (2015).

Overall we observe a good agreement between FWHM and  $FWHM_{ph}$  values, with  $<10\%$  fractional difference, which was our initial test goal. Only in the case of J1357 does the difference rise to 15%, although the large error bar in  $FWHM_{ph}$  makes the two values consistent within  $1\sigma$ . In any case, it should be borne in mind that J1357 experienced an outburst in April 2017 (Drake et al. 2017) and, therefore, the binary may have not returned to the pre-outburst quiescent state by the time of our ACAM observations. In that case, the  $FWHM_{ph}$  value would be underestimated because the accretion disc may not have time to reach the equilibrium radius (see e.g. Fig. 2 in Paper I for the long-term evolution of FWHM in V404 Cyg). Following from Paper III, we also present the  $EW_{ph}$  and  $FWHM_{ph}$  information in the form of a colour-colour diagram<sup>3</sup> in Figure 4. To guide the eye, lines of constant EW and FWHM, as computed from eq. 4-7, are overplotted.

As a further test, we have calculated synthetic magnitudes through the convolution of the BHXB spectra with the filter transmission curves. The results are again listed in Table 3 and plotted as blue circles in Figure 4, with open circles referring to synthetic magnitudes of individual spectra while filled circles to those of average spectra. We observe that line profile variability causes slight changes in the position of the blue open circles across the diagram. Since these fluctuations are sampled on short timescales ( $\sim 1$ -30 min), they are likely dominated by stochastic flickering rather than smooth orbital modulations. Interestingly, the displacements appear to follow lines of constant FWHM, suggesting that flickering is dominated by EW variations rather than changes in line width. This agrees with previous spectrophotometric studies of V404 Cyg where it was found that flaring activity is better traced by line flux than continuum flux, with the width and shape of the line profile remaining largely unaffected (Hynes et al. 2002, 2004).

The synthetic FWHM values ( $FWHM_{syn}$ ) presented in Table 3 are seen to differ from  $FWHM_{ph}$  by typically  $\sim 3$ -12%. On the other hand,  $FWHM_{syn}$  deviates by 3-6% from

<sup>3</sup> We note in passing a small error in Fig. 8 of Paper III, which appears flipped across the x-axis according to its label.

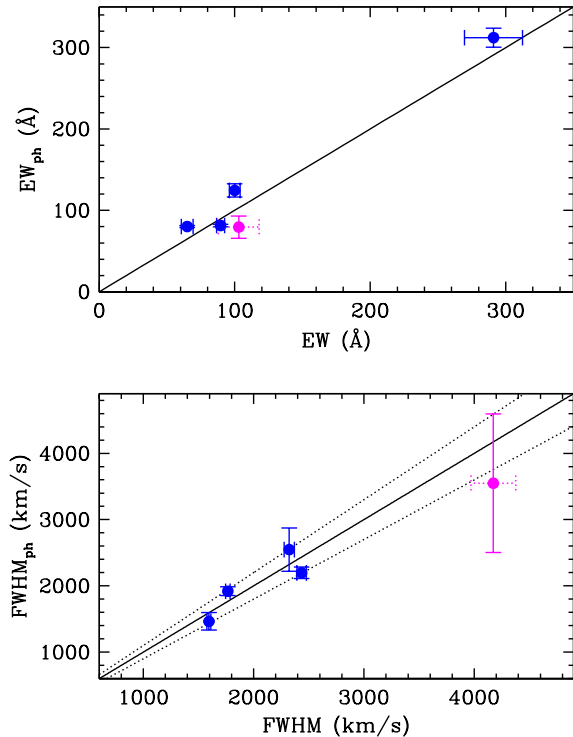


**Figure 3.** Top: Photometric EWs ( $EW_{ph}$ ) versus EW values measured from near-simultaneous spectra. Bottom: Photometric FWHMs ( $FWHM_{ph}$ ) versus FWHM values from spectra. The magenta points represent values for J1357 derived from a single photometric point (SNR $\sim 16$  per filter). In this case, due to the lack of simultaneous spectroscopy, we adopt EW and FWHM values from Mata Sanchez et al. (2015). The dotted lines represent the goal of  $\pm 10\%$  fractional limit in  $FWHM_{ph}$ .

the spectroscopic FWHM values. Since these are obtained from the same data but through different methods (synthetic photometry versus direct spectral line fitting), the latter discrepancies reflect our limitation in calibrating the photometric quantities  $EW_{ph}$  and  $FWHM_{ph}$  (Section 3.1). The result is not surprising, given the different transmission curves and central wavelengths of our actual filters compared to those of perfect ideal filters.

#### 4 SUMMARY AND OUTLOOK

The outcome of our feasibility study is summed up by Table 3 and Figures 3-4. The conclusions are summarised as follows:

- (1)  $H\alpha$  line widths can be measured to about  $\sim 10\%$  accuracy through images obtained with an adequate combination of filters. This becomes possible even at very faint luminosities, provided SNR $\approx 50$  is achieved in every filter. For example, in the case of J0422, with  $r = 21.3$ , SNR $\approx 50$  was acquired in all filters, leading to an 8% fractional difference between  $FWHM_{ph}$  and the (spectroscopic) FWHM.
- (2) Line width precision significantly better than  $\sim 10\%$  is

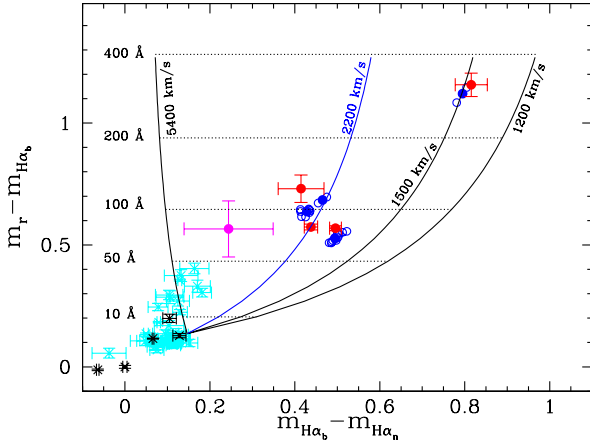


**Figure 4.** The  $H\alpha$  colour-colour diagram. The photometric colours of standard stars are represented by black asterisks, with the zero point defined by the A0V star BD +30 2355. Average photometric colours of BHs and field stars with  $\text{SNR} \geq 50$  are indicated by filled red circles and cyan crosses, respectively. For comparison, synthetic colours of individual GTC BH spectra are plotted as blue open circles, while blue filled circles represent synthetic colours from average spectra. The solid magenta circle depicts the photometric colours of Swift J1357-0933, as derived from a single set of images. Lines of constant EW, in the range 10–400 Å, and constant FWHM between 1200–5400  $\text{km s}^{-1}$  are also marked.

not always possible because of intrinsic fluctuations, mostly driven by flickering variability. As an example, very high SNR in the range  $\sim 150$ –200 was acquired for the bright targets A0620 and J1118 but this only results in  $FWHM_{ph}$  determinations with 9–10% fractional difference with respect to the spectroscopic FWHM values.

(3) As observed in Figure 4, flickering variability leads to EW fluctuations on  $\sim \text{min}$  timescales, with little variation in line FWHM. In any case, we have shown that these can be averaged out using a filter cycling strategy. This, in turn, allows considerable extension of the dynamic range and prevents saturation of relatively bright stars. For instance, our deep J0422 observation achieves an accumulated  $\text{SNR} \sim 50$  at  $r \sim 21$  while millimag precision is obtained for field stars with  $r \sim 16$ . Furthermore, filter cycling provides light curve information (Figure 2) which becomes extremely useful to identify short-period CVs through the presence of  $\sim 2$ –3 mag deep eclipses. As stated in Paper III, these are the main Galactic sources of BHXB contamination at very large FWHM values  $\geq 2200 \text{ km s}^{-1}$ .

(4) In the case of the faintest target J1859 ( $r \simeq 22$ ) our observations prove that BHXBs can still be recovered with  $\text{SNR} \sim 35$ . This is equivalent to the SNR expected at  $r=23$  for a survey goal of  $\text{SNR}=50$  at  $r=22$ . In other words, the J1859 observation demonstrates that BHXBs with  $FWHM \geq 2200 \text{ km s}^{-1}$  can be detected with 3% photometry at  $r=23$ . According to Paper III, such survey depth would lead to  $>100$  new BHXBs in an area of 1 kilo square deg on the Galactic Plane, an order of magnitude improvement over the current population.

(5) The single photometric observation of J1357 also demonstrates that BHXBs with very large  $FWHM \sim 3000$ –4000  $\text{km s}^{-1}$  can be identified above the 2200  $\text{km s}^{-1}$  limit

even at modest  $\text{SNR} \sim 16$ . For a survey goal of  $\text{SNR}=50$  at  $r=22$  this implies that J1357-like binaries can be detected down to  $r \sim 24.5$ . As shown by Figure 9 in Paper III, these are all short period BHXBs and might represent the bulk of the hidden hibernating population. It should be noted that, because line width increases at short orbital periods, our FWHM selection method is actually biased towards detecting short period quiescent BHs. This is opposed to X-ray/radio survey efforts that are biased to selecting long period BHs since luminosity decreases with period (Wu et al. 2010; Kneivitt et al. 2014). Furthermore, since FWHM increases with binary inclination as well (eq. 8 in Paper I) our strategy is also biased towards detecting high inclination BHs. This makes another interesting outcome, given the current paucity of BHXBs with  $i \gtrsim 75^\circ$  due to X-ray selection effects (Narayan & McClintock 2005).

(6) Finally, Figure 4 shows that field stars appear conveniently segregated from BHXB targets. G and early-K type stars tend to cluster at  $EW \simeq 0$ , near the focus point where lines of equal FWHM converge. Earlier spectral types lie along a tail leftwards of the focal point while late-K and M stars define a vertical stream along  $FWHM \simeq 5400 \text{ km s}^{-1}$ , driven by the appearance of TiO molecular bands on each side of  $H\alpha$ , which effectively fake extremely broad emission profiles.

An important asset of our filter combination is the clean separation of  $H\alpha$  emitters from field stars, independently of interstellar reddening. This is possible because all filters are centered at the rest wavelength of  $H\alpha$ . In fact, a relative displacement between the central wavelength (CWL) of the  $r$ -band and  $H\alpha_b$  filters would lead to a vertical shift in the position of reddened field stars, while a displacement between the CWLs of the  $H\alpha_b$  and  $H\alpha_n$  filters would result in a horizontal shift. We have quantified this by running simulations using idealized nearly-squared filters with effective widths 37 Å, 150 Å and 350 Å, and the Jacoby library of standard stars (Jacoby et al. 1984), reddened by several amounts. We here adopt  $H\alpha_n$  and  $H\alpha_b$  filters that are broader than NOT21 and NOT29, motivated by the scientific requirements presented Paper III. We also limit the FWHM of the  $r$ -band filter to 350 Å in order to avoid the main telluric bands and strong airglow emission lines such as O I 6300 Å. We find that, for extreme reddenings  $E(B-V)=3$ , a displacement of +30 Å (–30 Å) between the CWL of  $H\alpha_b$  and that of the  $r$ -band translates into a vertical shift of +0.05 (–0.05) mags in the diagram. Similarly, a horizontal shift of +0.05 (–0.05) mags is obtained if the CWL of  $H\alpha_n$  is displaced by +30 Å (–30 Å) with respect to that of the  $H\alpha_b$  filter. These shifts are very modest and imply that BH candidates (and other  $H\alpha$  emitters), detected by  $H\alpha$  filters with  $\pm 15$  Å tolerance in CWL, will not be mixed up with countless field stars, even along sight-lines of substantial interstellar extinction.

To conclude the paper we now focus our attention on opportunities presented by our photometric system to disentangle other populations of compact stars and  $H\alpha$  emitters.

#### 4.1 Other Galactic Populations in HAWKS

*HAWKS*, a survey concept based on these filters, will not only boost the statistics of hibernating BHs. It will also deliver a full census of  $H\alpha$  emitters and other Galactic populations

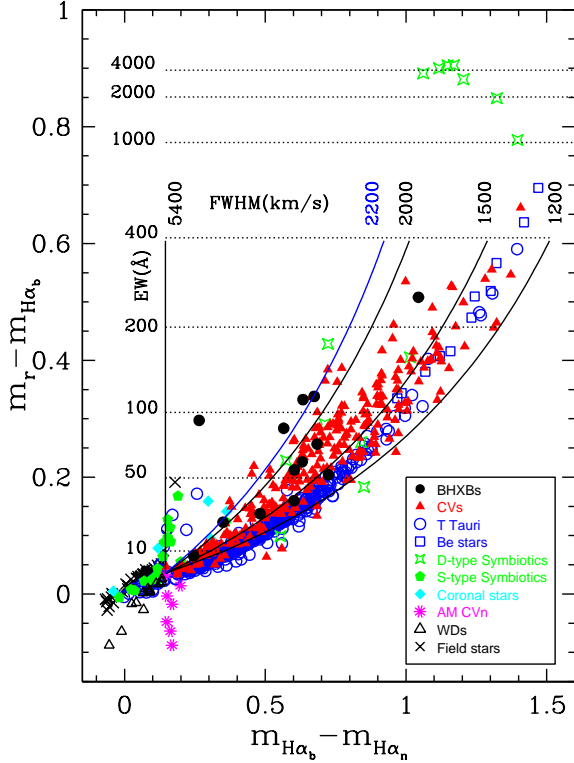


**Figure 5.**  $H\alpha$  colour-colour diagram showing synthetic colours of BHXBs and field stars, together with other Galactic populations of interest. The list of BHXBs contains spectra from this paper together with others presented in Paper I and Mata Sánchez et al. (2015). Other spectral samples have been selected from the SDSS and IPHAS catalogues. This figure has been produced using a set of idealised nearly-squared filters centered at 6563 Å and effective widths 37 Å, 150 Å and 350 Å. Lines of constant EW and FWHM are represented as in Figure 4.

to unprecedented depths. *HAWKs* will effectively unfold into a catalogue of dynamical BHs (the *BLACK – HAWKs*) plus other catalogues of different “flavours” (the “*COLOURED*”–*HAWKs*), broadly classified by their FWHM-EW positions in the  $H\alpha$  colour-colour diagram. This is illustrated in Figure 5, where synthetic colours of several Galactic populations of interest are represented (note that this figure has been produced using the same idealised filters referred to above rather than the actual MR661, NOT21 and NOT21 filters employed in Figure 4).

For example, *HAWKs* will produce a new census of symbiotic stars i.e. long period accreting binaries with a compact star embedded in the wind of an evolved giant companion (Belczyński et al. 2000). D-type symbiotics tend to cluster at very large EWs  $>1000$  Å, a region also populated by PNe. S-type symbiotics, on the other hand, are dominated by the spectrum of the donor and distribute along the main stellar locus defined by field stars. The size of the symbiotic population is very uncertain ( $\approx 10^3 - 10^5$ ) with only  $\sim 200$  binaries currently known, 19 of which have been revealed by IPHAS (Rodríguez-Flores et al. 2014). *HAWKs*, with its deeper survey limit, can make a large impact on the field.

Young stellar objects (YSOs) of different types, such as T Tauri, Herbig Haro objects or classical Be stars, are characterized by narrow FWHMs in the range  $\sim 100$ - $500$   $\text{km s}^{-1}$  and, thus, will concentrate at the lower FWHM limit of the diagram. A much expanded sample will allow important questions on YSO physics, such as the evolution of accretion rates and the survival of protoplanetary discs, to be addressed (Barentsen et al. 2011; Venuti et al. 2018).

On the other hand, CVs do spread over a much wider range of FWHM values. Those with  $\text{FWHM} \geq 2200$   $\text{km s}^{-1}$  will reveal themselves as short-period eclipsing WZ Sge and minimum period-bouncers, of considerable interest for the study of CV evolution (e.g. Littlefair et al. 2008; Gänsicke et al. 2009). CVs with FWHM in the range 1500-2200  $\text{km s}^{-1}$  will be mostly eclipsing too, allowing for precise white dwarf mass determinations and the identification of possible SN Ia progenitors (Maoz, Mannucci & Nelemans 2014). Within this parameter space, the sample will also reveal quiescent NS X-ray binaries and millisecond pulsars (some will be eclipsing), ideal targets to explore the upper bound of neutron star masses and the equation of state of ultra-dense matter (e.g. Linares et al. 2018). For example, assuming a maximum NS mass of  $2.3 M_{\odot}$  (Ruiz et al. 2018) the *photometric mass function* equation (eq. 2 in Paper III) implies that all NSs with  $\text{FWHM} > 2200$   $\text{km s}^{-1}$  must have orbital periods shorter than  $\approx 3.6$  h and will be mostly high inclination. Therefore, they can be easily spotted through eclipses, ellipsoidal modulation or irradiation variability in light curves spanning less than 4 hr.

Beyond  $H\alpha$  emitters, the colour-colour diagram will also reveal populations of AM CVn systems i.e. ultra-compact binaries with two (semi-)degenerate white dwarfs (Solheim 2010). A combination of hydrogen deficiency, together with the presence of He I emission lines, places these systems in a vertical stream at negative EWs. The region will also contain ultra-compact X-ray binaries with accreting NSs (Sengar et al. 2017). Ultra-compact binaries are very faint and rare, with a space density comparable to that of BHXBs, and thus only a few tens are currently known (Carter et al. 2013). Nonetheless, they are key systems to constrain common envelope parametrizations and, hence, close binary evolution models (Ivanova et al. 2013). Furthermore, they are predicted to be the brightest persistent GW sources and some will even become verification sources for LISA (Korol et al. 2017; Kupfer et al. 2018).

Finally, because our narrow band filters are sensitive to gravity effects, *HAWKs* will be able to discriminate between DA white dwarfs (WDs) and A-B main sequence stars. WDs appear on a separate track under the main stellar locus, with DA2-3 types offset by as much as  $-0.1$  mag in  $(m_r - m_{H\alpha_b})$  colour. With a survey depth of  $r = 24$  (5% photometry) *HAWKs* can extend the number of DA WD discoveries to much larger volumes than previous surveys, including Gaia (Hollands et al. 2018). This will result in new constraints on their space density, scale height and merger rates (Giammichele et al. 2012; Kilic et al. 2018). The sample will likely contain new pulsating (ZZ Ceti) stars, WD binaries and WDs with planetary debris discs (Limoges et al. 2015; Farihi 2016), which would be disclosed by follow-up studies.

Synergies with existing and next generation surveys will be important to further disentangle and characterize these populations. For example, late-type T Tauri and coro-



nal stars can be displaced rightward into the BHXB region due to the confluence of broad molecular bands and narrow H $\alpha$  emission. However, these are nearby objects which will be flagged by Gaia parallaxes and near-IR excesses. Contaminating symbiotic stars, on the other hand, can be identified from mid-IR colours granted by the extended all-sky survey NEOWISE (Mainzer et al. 2014). Spitzer/GLIMPSE (Churchwell et al. 2009) and NEOWISE mid-IR colours will also single out YSOs of different types through the presence of circumstellar gas/dust emission. Global photometric surveys such as Pan-STARRS (Kaiser et al. 2010), BlackGEM (Roelfsema et al. 2016) and the *Large Synoptic Survey Telescope* LSST (Abell et al. 2009) will feed in broad optical colours and variability information to help constrain spectral energy distributions (SEDs) and orbital periods. The ground-breaking sensitivity of the *Square Kilometer Array* SKA (Carilli & Rawlings 2004) and pathfinders, the *James Webb Space Telescope* JWST (Gardner et al. 2006) and the *extended ROentgen Survey with an Imaging Telescope Array* eROSITA (Merloni et al. 2012) will provide transient properties and multiwavelength fluxes to build full SEDs of all targets. Gaia will complement with distances and, therefore, luminosities for the brightest of these objects. Meanwhile, wide-field multi-object spectrographs such as *2dF*, WEAVE (Dalton et al. 2012) or 4MOST (de Jong et al. 2016) will furnish optical classification spectra of subsets of H $\alpha$  emitters in different FWHM bands. Finally, next generation ELTs will allow detailed spectroscopic studies of selected targets at the faint magnitude end and dynamical confirmation of new BH candidates.

## ACKNOWLEDGEMENTS

Based on observations made with the GTC and WHT telescopes under Director's Discretionary Time GTC/WHT/2017-089 of Spain's Instituto de Astrofísica de Canarias. We would like to thank T. Muñoz-Darias, P.A. Charles and T. Maccarone for many interesting discussions on the survey strategy and useful comments to the manuscript. We are very grateful to J. Calvo and the IAC mechanical engineers team for manufacturing a ring adaptor that allowed mounting filter MR661 in ACAM. Also to C. Benn and N. O'Mahony for their advice in the design of the adaptor ring and to T. Augusteijn, J. Telting and the NOT institute for the support and flexibility in providing us with the H $\alpha$  filters #21 and #29. Observing support by ING support astronomers C. Fariña, R. Karjalainen, M. Karjalainen and L. Domínguez is gratefully acknowledged. We also thank A. Cabrera and J. Méndez for the flexibility and coordination in scheduling these DDT observations. We are grateful to J.M. Corral-Santana for providing us with spectral samples of H $\alpha$  emitting stars. JC acknowledges support by the Spanish Ministry of Economy, Industry and Competitiveness (MINECO) under grants EUIN2017-89095 and AYA2017-83216-P. MAPT also acknowledges support by MINECO under the Ramón y Cajal Fellowship RYC-2015-17854. MOLLY software developed by T. R. Marsh is gratefully acknowledged.

## REFERENCES

- Abbott, B.P. et al. (LIGO Scientific Collaboration and Virgo Collaboration), 2016a, *Phys. Rev. Lett.*, 116, 061102
- Abbott, B.P. et al. (LIGO Scientific Collaboration and Virgo Collaboration), 2016b, *Phys. Rev. Lett.*, 116, 241103
- Abbott, B.P. et al. (LIGO Scientific Collaboration and Virgo Collaboration), 2017, *Phys. Rev. Lett.*, 118, 221101
- Abbott, B.P. et al. (LIGO Scientific Collaboration and Virgo Collaboration), 2017, *Phys. Rev. Lett.*, 119, 141101
- Abbott, B.P. et al. (LIGO Scientific Collaboration and Virgo Collaboration), 2017, *ApJ*, 851, L35
- Abell, P. A. et al. (LSST Science Collaboration), 2009, *LSST Science Book, Version 2.0*, arXiv:0912.0201
- Barentsen G. et al., 2011, *MNRAS*, 415, 103
- Belczyński K., Mikolajewska J., Munari U., Ivison R.J., Friedjung M., 2000, *A&AS*, 146, 407
- Belczyński K. et al., 2010, *ApJ*, 714, 1217
- Carilli C.L., Rawlings S., 2004, *New Astron. Rev.*, 48, 979
- Carter P.J. et al., 2013, *MNRAS*, 429, 2143
- Casares J., 2015, *ApJ*, 808, 80 (Paper I)
- Casares J., 2016, *ApJ*, 822, 99 (Paper II)
- Casares J., 2018, *MNRAS*, 473, 5195 (Paper III)
- Casares J., Jonker P.G., 2014, *Space Sci. Rev.*, 183, 223
- Casares J., Negueruela, I., Ribó, M., Ribas I., Paredes J.M., Hertero A., Simón-Díaz S., 2014, *Nature*, 505, 378
- Casares J., Jonker P.G., Israelian, G., 2017, *X-ray Binaries in Handbook of Supernovae*, A.W. Alsabti and P. Murdin editors, ISBN 978-3-319-21845-8. Springer, p.1499 (arXiv:1701.07450)
- Churchwell E. et al., 2009, *PASP*, 121, 213
- Corral-Santana J.M., Casares J., Muñoz-Darias T., Bauer F.E., Martínez-Pais I.G., Russell D.M., 2016, *A&A*, 587, A61
- Dalton G. et al., 2012, *Proc. of the SPIE*, 8446, 12
- Drake A.J., et al. 2017, *The Astronomer's Telegram*, 10297
- de Jong, S.R. et al., 2016, in *Proc. SPIE*, Vol. 9908
- Drew J. et al., 2005, *MNRAS*, 362, 753
- Farihi J., 2016, *New Astronomy Rev*, 71, 9
- Fryer C.L., Belczynski K., Wiktorowicz G., Dominik M., Kalogera V., Holz D.E., 2012, *ApJ*, 749, 91
- Gänsicke B.T. et al., 2009, *MNRAS*, 397, 217
- Gardner J.P., 2006, *Space Sci. Rev.*, 123, 485
- Giammichele N., Bergeron P., Dufour P., 2012, *ApJS*, 199, 29
- Grindlay J.E. et al., 2015, *ApJ*, 635, 920
- Grudzinska M. et al., 2015, *MNRAS*, 452, 2773
- Hollands M.A., Tremblay P.-E., Gänsicke B.T., Gentile-Fusillo N.P., Toonen S., 2018, *MNRAS*, 480, 3942
- Hynes R.I. et al., 2002, *MNRAS*, 330, 1009
- Hynes R.I. et al., 2004, *ApJ*, 611, L125
- Ivanova N. et al., 2013, *A&A Rev.*, 21, 59
- Jacoby G.H., Hunter D.A., Christian C.A., 1984, *ApJS*, 56, 257
- Jonker P.G. et al., 2011, *ApJS*, 194, 18
- Kaiser N. et al., 2010, in *Proc. SPIE*, Vol. 7733, *Ground-based and Airborne Telescopes III*, ed. L.M. Stepp, R. Gilmozzi & H.J. Hall
- Kilic M., Hambly N.C., Bergeron P., Genest-Beaulieu C., Rowell N., 2018, *MNRAS*, 479, L113
- Kneivitt G., Wynn G.A., Vaughan S., Watson M.G., 2014, *MNRAS*, 437, 3087
- Korol V., Rossi E.M., Groot P.J., Nelemans G., Toonen S., Brown A.G.A., 2017, *MNRAS*, 470, 1894
- Kupfer T., et al., 2018, *MNRAS*, 480, 302
- Landolt A.U., 1992, *AJ*, 104, 340
- Limoges M.-M., Bergeron P., Lépine S., 2015, *ApJS*, 219, 19
- Linares M., Shahbaz T., Casares J., 2018, *ApJ*, 859, 54
- Littlefair S.P., Dhillon V.S., Marsh T.R., Gänsicke B.T., Southworth J., Baraffe I., Watson C.A., Copperwheat C., 2008, *MNRAS*, 388, 1582



- Mainzer A. et al., 2014, ApJ, 792, 30
- Maoz D., Mannucci F., Nelemans G., 2014, ARA&A, 52, 107
- Marsh T.R., 1989, PASP, 101, 1032
- Mata Sánchez D, Muñoz-Darias T., Casares J., Corral-Santana J.M., Shahbaz T., 2015, MNRAS, 454, 2199
- Merloni A. et al., 2012, MPE document, ed. S. Allen, G. Hasinger & K. Nandra, arXiv:1209.3114
- Mirabel I.F., 2017, New Astron. Rev., 78, 1
- Narayan R., McClintock J.E., 2005, ApJ, 623, 1017
- Podsiadlowski Ph., Rappaport S., Han Z., 2003, MNRAS, 341, 385
- Repetto S., Igoshev A., Nelemans G., 2017, MNRAS, 467, 298
- Rodríguez-Flores E.M., Corradi R.L.M., Mampaso A., García-Alvarez D., Munari U., Greimel R., Rubio-Díez M.M., Santander-García M., 2014, A&A, 567, A49
- Roelfsema R. et al., 2016, in Proc. SPIE, Vol. 10012
- Rogel A.B., Lugger P.M., Cohn H.N., Slavin S.D., Grindlay J.E., Zhao P., Hong J., 2006, ApJS, 163, 160
- Ruiz M., Shapiro S.L., Tsokaros A., 2018, PhRvD, 97, 021501
- Sengar R., Tauris T.M., Langer N., Istrate A.G., 2017, MNRAS, 470, L6
- Stetson P.B., 1990, PASP, 102, 932
- Solheim J.-E., 2010, PASP, 122, 1133
- Tauris T.M., van den Heuvel E.P.J., 2006, *Formation and evolution of compact stellar X-ray sources* in Compact stellar X-ray sources. W. Lewin and M. van der Klis editors. Cambridge Astrophysics Series, No. 39, p.623
- Torres M.A.P. et al., 2014, MNRAS, 440, 365
- Torres M.A.P., Jonker P.G., Miller-Jones J.C.A., Steeghs D., Repetto S., Wu J., 2015, MNRAS, 450, 4292
- Ugliano M., Janka H.-T., Marek A., Arcones A., 2012, ApJ, 757, 69
- Venuti L. et al., 2018, A&A, 609, 10
- Wang C., Jia K, Li X.-D., 2016, MNRAS, 457, 1015
- Wevers T. et al., 2017, MNRAS, 466, 163
- Witham A.R. et al., 2006, MNRAS, 369, 581
- Wu Y.X., YU W., Li T.P., Maccarone T.J., Li X.D., 2010, ApJ, 718, 620
- Zurita C., Casares J., Shahbaz T., 2003, ApJ, 582, 369

**Table 1.** Observing log

Target	Date	r	H $\alpha$ <sub>b</sub>	H $\alpha$ <sub>n</sub>	Spectra
SWIFT J1357.2-0933	16 Feb 2018	30s	300s	600s	–
GRO J0422+320	17 Feb 2018	2x20s/30s/2x60s	4x200s	100s/400s/2x200s	2x1200s (OSIRIS)
A 0620-00	”	6x5s	5x30s	5x30s	12x60s (OSIRIS)
XTE J1118+480	”	2x5s/14x30s	2x30s/14x60s	30s/2x60s/10x120s/2x200s	8x300s (OSIRIS)
XTE J1859+226	20 June 2018	4x60s	3x270s/250s	206s/420s/3x600s	2x1800s (OSIRIS)
BD+30 2355 (A0 V)	17 Feb 2018	0.2s	5s	10s	30s (ACAM)
FEIGE 15 (A1 IV)	”	0.2s	5s	10s	30s (ACAM)
SA95 15 (G8 V)	”	1s	8s	30s	150s (ACAM)
SA95 16 (K7 V)	”	2s	8s	30s	150s (ACAM)

**Table 2.** Photometric versus synthetic H $\alpha$  colours of standard stars. Typical errors are at the millimag level.

STAR	PHOTOMETRIC COLOURS			SYNTHETIC COLOURS	
	$m_r^\dagger$	$m_r - m_{H\alpha_b}$	$m_{H\alpha_b} - m_{H\alpha_n}$	$m_r - m_{H\alpha_b}$	$m_{H\alpha_b} - m_{H\alpha_n}$
BD+30 2355 (A0 V)	9.54	0	0	0.10	0.03
FEIGE 15 (A1 IV)	9.32	-0.01	-0.06	0.06	-0.01
A0620-C1 (G5 V) $^{\dagger\dagger}$	15.46	0.13	0.13	0.12	0.10
SA95 15 (G8 V)	9.83	0.12	0.07	0.14	0.10
SA95 16 (K7 V)	12.46	0.20	0.11	0.19	0.13

$^\dagger$  These are instrumental magnitudes. Comparison with calibrated r-band magnitudes indicate  $r = m_r + 1.1$ .

$^{\dagger\dagger}$  Photometric magnitudes and colours are weighted averages over all filter cycles.

**Table 3.** Photometric/synthetic EW and FWHM values compared to those measured from near-simultaneous spectra. Errorbars represent  $1\sigma$  confidence intervals.

Target	$m_r$	SNR	$r^\dagger$	EW (Å)	EW <sub>ph</sub> (Å)	EW <sub>syn</sub> (Å)	FWHM (km/s)	FWHM <sub>ph</sub> (km/s)	FWHM <sub>syn</sub> (km/s)
GRO J0422+320	19.8	50	21.3	291±21	312±12	290±5	1595±18	1464±132	1496±20
A 0620-00	16.0	165	17.2	65±4	80±1	70±1	1766±20	1919±66	1839±11
XTE J1118+480	18.0	150	19.1	90±3	81±1	98±1	2435±42	2197±86	2353±15
XTE J1859+226	20.6	35	21.9	100±4	124±8	111±1	2323±47	2548±327	2236±64
SWIFT J1357.2-0933 <sup>††</sup>	19.6	16	20.9	103±15	79±14	–	4173±203	3548±1045	–

<sup>†</sup> Continuum r-band magnitude, calibrated from the instrumental magnitude  $m_r$  and corrected for the contribution of the H $\alpha$  flux following  $r = m_r + 1.1 + 2.5 \log(1 + EW/W_r)$ .

<sup>††</sup> The quoted values for EW and FWHM are obtained from 2014 spectra presented in [Mata Sánchez et al. \(2015\)](#).



This paper has been typeset from a T<sub>E</sub>X/L<sup>A</sup>T<sub>E</sub>X file prepared by the author.